RSC Advances

PAPER

View Article Online
View Journal | View Issue

Cite this: *RSC Adv.*, 2025, **15**, 34310

Comparison of adsorption mechanisms of tungstate ions on different clay minerals

Yang Peng,[abcd] Yuping Chen,[e] Hao Wu,[d] Ziqin Wang,[abc] Liu Yang,[d] Jiale Chen,[b] Xinjuan Chen,[b] Fu Liu,[b] Nan Wang,[b] Yuru Dong,[abc] Jie Liu,[abc] Jie Xiao[abc] and Ming Chen *[abc]

Tungsten, widely used in industry, can cause ecological risks like soil degradation and plant growth inhibition due to its migration and accumulation in the environment. Studying its adsorption mechanisms helps understand its transformation laws, accurately evaluate ecological risks, and develop control strategies. This study combines first-principles simulations based on DFT (density functional theory) with experiments to explore the different adsorption behaviors of tungsten (WO_4^{2-}) on three clay minerals: kaolinite, montmorillonite, and illite. Adsorption experiments show that lowering the solution pH, increasing the initial concentration, and extending the adsorption time all enhance WO_4^{2-} adsorption on the three minerals. A higher pH increases the negative charge on the minerals' surfaces, boosting electrostatic repulsion and reducing WO_4^{2-} adsorption. Adsorption kinetics and isotherm studies indicate that the adsorption process on the three minerals follows pseudo-second-order kinetics and the Langmuir model, suggesting chemisorption dominance. The adsorption rate for WO_4^{2-} is illite > kaolinite > montmorillonite, while the adsorption capacity at equilibrium is montmorillonite > kaolinite > illite. First-principles studies reveal that WO_4^{2-} forms one Al–O coordination bond (1.889 Å) on kaolinite (001), two Si–O bonds (1.799 Å, 1.889 Å) on montmorillonite, and two Si–O bonds (both 1.800 Å) on illite (001). The adsorption of WO_4^{2-} on the (001) faces of these minerals is mainly chemisorption, with adsorption energies of −166.94 kJ mol^{-1} (kaolinite), −178.52 kJ mol^{-1} (montmorillonite), and −112.65 kJ mol^{-1} (illite). WO_4^{2-} adsorbs most easily on montmorillonite (001) due to its lowest adsorption energy and highest stability, followed by kaolinite (001), and least easily on illite (001).

Received 17th June 2025
Accepted 11th September 2025

DOI: 10.1039/d5ra04306a

rsc.li/rsc-advances

1 Introduction

Tungsten is a strategic non-renewable metal resource in the national economy and modern defense due to its stable chemical properties, high hardness, and good thermal and electrical conductivity, leading to its widespread use in aerospace, metallurgy, electrochemical devices, the military, manufacturing, and electronics.[1–4] As global tungsten demand grows, so does the mining volume. Waste rock and tailings from tungsten mining and smelting containing tungsten enter the soil *via* weathering and leaching, causing pollution.[5–8] When soil heavy metals reach certain concentrations, they can migrate into water, air, and crops, ultimately posing direct or indirect risks to human health.[9–12]

Tungsten compounds in soil were long thought to be stable, a perception that has resulted in limited research attention being directed toward this element. Over the past decade, however, studies have demonstrated that tungsten can oxidize into soluble, reactive tungstate (WO_4^{2-}) ions under natural conditions, thereby complicating its environmental behavior.[13,14] Research findings indicate that in acidic soils, tungsten occurs in the form of polytungstates, whereas in alkaline soils, it predominantly exists as WO_4^{2-} ions. Tungsten exhibits greater activity and mobility in alkaline soil environments. Similar to other metal anions, the distribution, mobility, and bioavailability of tungsten are pH-dependent.[15–17] Bolan *et al.*[18] emphasized that the solubility and mobility of tungsten are also influenced by its interactions with positively charged iron, aluminum, and manganese oxides, as well as silicate clay minerals. These interactions, in turn, are affected by the variable charge components in soils or sediments. The environmental behavior and potential risks of tungsten in soil have gradually attracted

[a]*Jiangxi Provincial Key Laboratory of Environmental Pollution Prevention and Control in Mining and Metallurgy, Ganzhou 341000, Jiangxi Province, PR China. E-mail: jxlgcm@163.com; Tel: +86 797 8312776*

[b]*College of Resource and Environmental Engineering, Jiangxi University of Science and Technology, Ganzhou 341000, Jiangxi Province, PR China*

[c]*Cooperative Innovation Center Jointly Established by the Ministry and the Ministry of Rare Earth Resources Development and Utilization, Ganzhou 341000, Jiangxi Province, PR China*

[d]*School of Ecological Construction and Environmental Protection, Jiangxi Environmental Engineering Vocational College, Ganzhou 341000, Jiangxi Province, PR China*

[e]*School of Intelligent Manufacturing and Materials Engineering, Gannan University of Science and Technology, Ganzhou 341000, Jiangxi Province, PR China*

the attention of scientific and technological workers, who have begun to explore the adsorption characteristics of tungstate (WO_4^{2-}) on soil mineral components, which is crucial for clarifying the mobility of WO_4^{2-} in soil and water systems. Layered silicate minerals are the most common and largest proportion of clay minerals in soil. They have the characteristics of large specific surface area, high chemical and mechanical stability, interlayer structure and high cation exchange capacity, and are important factors affecting the transformation and migration of heavy metal ions in the environment.[19–21] Common layered silicate minerals include kaolinite, illite, montmorillonite, *etc.* Sen Tuna and Braida[22] discovered that as pH increased from 3 to 6, the adsorption of W by kaolinite decreased from 87% to 65%. For other layered silicates, the adsorption of W in montmorillonite and illite also decreases with the increase of pH. Iwai *et al.*[23] investigated the adsorption characteristics of WO_4^{2-} on soil clay minerals such as bauxite trihydrate, iron (oxygen) oxides, feldspar and montmorillonite, and analyzed the influence of pH value on the competitive adsorption of WO_4^{2-} with PO_4^{3-} and MoO_4^{2-}. They found that the adsorption affinity of WO_4^{2-} was in the order of bauxite trihydrate > feldspar > montmorillonite. Gianniantonio Petruzzelli *et al.*[24] studied the adsorption and desorption processes of tungstate ions in three types of soils in the Mediterranean region. They found that the adsorption of tungstate could be described by the Langmuir type equation. The pH value was the main soil property regulating adsorption/desorption, and the soil with a slightly acidic pH value had the largest adsorption capacity. The desorption capacity of alkaline soil is the greatest. The above results indicate that clay minerals, due to their active surface charge, large specific surface area and simple crystal structure, are an important component affecting the transformation and migration of heavy metal ions in the environment. However, the current research mainly focuses on the influence law of the adsorption behavior of tungsten by clay minerals. There are few reports on the influence mechanism of tungsten adsorption by clay minerals and most of them are conventional experimental studies, which cannot be explained from the microscopic perspectives such as molecules and atoms, resulting in the inability to accurately describe the influence mechanism of the interaction between tungsten and the surface of clay minerals.

Density functional theory is a fundamental quantum chemistry research that can obtain microscopic information at the atomic and molecular levels, effectively compensating for the shortcomings of traditional experimental methods. At present, the first-principles method has been successfully applied in research fields such as lattice defect theory,[25] ionic solvation effect,[26,27] and surface and interface adsorption of clay minerals.[28] For instance, He *et al.*[29] conducted a systematic first-principles molecular dynamics (FPMD) simulation to investigate that tungsten exhibited a 5× coordination in the WO_4^{2-} and HWO_4^- systems, while it transformed to a 6× coordination in the H_2WO_4 system. Chi[30] utilized quantum chemical calculations to point out that the adsorption surface active centers of the substituted structures of montmorillonite, halloysite, and kaolinite have a greater adsorption capacity for cations than the adsorption active centers of the cross-section residual bonds. Their adsorption capacity for cations is as follows: montmorillonite > halloysite > kaolinite. Quantum chemical calculations can effectively obtain the microstructure and mechanism of WO_4^{2-} adsorption on the surface of clay minerals, and also evaluate the adsorption energy of clay minerals to adsorb WO_4^{2-}, which can provide guidance for the migration and diffusion of WO_4^{2-} in soil.

This paper takes three common clay minerals (kaolinite, montmorillonite, and illite) and WO_4^{2-} as the research objects. Through the combination of first-principles and experiments, the differences in the adsorption behavior of kaolinite, montmorillonite, and illite for WO_4^{2-} are studied, and the mechanism of the adsorption behavior of WO_4^{2-} on the surface of clay minerals is clarified from a microscopic perspective. These findings are conducive to clarifying the migration and transformation laws of tungsten in the soil environment and providing theoretical support for the formulation of tungsten pollution prevention and control strategies.

2 Experimental and research methods

2.1 Samples and test methods

2.1.1 Test samples and reagents. The samples required for the test are shown in Table 1. The clay minerals used in the test, kaolinite, were from Shanghai Aladdin Reagent Co., Ltd, montmorillonite from Shanghai RON Chemical Technology Co., Ltd, and illite from Shanlin Shiyu Mineral Co., Ltd. All of them were of analytical purity. The remaining reagents used in this study were all of analytical grade and provided by Shanghai Aladdin Reagent Co., Ltd.

2.1.2 Adsorption test method. The static adsorption method was adopted to study the adsorption performance of different clay minerals for WO_4^{2-} under different pH values, different adsorption times, different initial ion concentrations and other conditions. The specific steps of the adsorption test are as follows: take 0.05 g ± 5 mg of each of the three clay minerals and place them respectively in 50 mL centrifuge tubes, then divide them into three groups: ① montmorillonite group; ② kaolinite group; ③ illite group, 35 mL of sodium tungstate solution with different initial pH and concentrations was added to each of the three groups of centrifuge tubes for adsorption experiments. The centrifuge tubes filled with samples were placed in a constant temperature shaker, and the rotational speed was adjusted to 200 rpm for oscillation at room temperature. The experiments were designed to sample the three groups of samples at regular intervals with time gradients of 10 min, 30 min, 60 min, 120 min, 240 min, 360 min, 720 min, 1440 min and 2880 min respectively. Before all the supernatants are transferred to the centrifuge tubes, they need to be transferred through a 0.45 μm filter membrane using a disposable syringe. The concentration of WO_4^{2-} in the filtrate is tested by Inductively Coupled Plasma Optical Emission Spectrometry (ICP; ULTIMA2, HORIBA Trading (Shanghai) Co., Ltd). The calculation method of the adsorption capacity of WO_4^{2-} is shown in formula (1):

Table 1 Experimental samples and reagents

Drug name	Molecular formula	Molecular weight	Manufacturer
Sodium tungstate	$Na_2WO_4 \cdot 2H_2O$	329.85	Shanghai Aladdin Reagent Co., Ltd
Montmorillonite	$Al_2O_9Si_3$	282.21	Shanghai RON Chemical Technology Co., Ltd
Illite	$K_{0.75}Na_{0.04}Ca_{0.01}$ $Al_{2.04}(Si_{3.13}Al_{0.87})O_{10}(OH_{1.86}O_{0.14})$	390.79	Shanlin Shiyu Mineral Resources Co., Ltd
Kaolinite	$Al_2O_3 \cdot SiO_2 \cdot 2H_2O$	258.16	Shanghai Aladdin Reagent Co., Ltd
Hydrochloric acid	HCl	36.46	Shanghai Aladdin Reagent Co., Ltd
Sodium hydroxide	NaOH	40.00	Shanghai Aladdin Reagent Co., Ltd

$$q = V(C_0 - C_K)/m \quad (1)$$

Among these, q denotes the adsorption capacity, with the unit: mg g^{-1}; V represents the volume of the solution in the adsorption reaction, unit: L; C_0 is the initial concentration of WO_4^{2-} in the solution prior to the reaction, unit: mg L^{-1}; C_K stands for the concentration of WO_4^{2-} when the reaction reaches equilibrium, unit: mg L^{-1}; and m refers to the amount of clay mineral used, unit: g. All results are expressed as the mean value.

2.2 DFT calculation

2.2.1 Simulation methods and models. The DFT calculation is based on the plane wave pseudopotentia density functional theory. The relevant calculations are carried out using the Castep module in the Material Studio software. The main dissociation surface (001) surface of three different clay mineral particles (kaolinite, montmorillonite and illite) is studied, and three minerals, namely kaolinite, montmorillonite and illite, are established respectively. According to the molecular formulas of the clay mineral samples in Table 1, it can be known that illite is potassium illite, and kaolinite and montmorillonite are pure kaolinite and pure montmorillonite respectively. Moreover, clay minerals have a certain buffering effect. When the pH solution is ≤4, they will adsorb H atoms, causing the pH solution to tend to 4 and remain stable, which affects the adsorption effect of clay minerals on WO_4^{2-}. To compare with the hydroxyl surface of kaolinite (001), the hydroxyl surface of montmorillonite (001) and the hydroxyl surface of potassium illite (001) were selected for the convenience of comparison among the three. The surface structure of the minerals is shown in Fig. 1.

Under the generalized gradient approximation (GGA), the GGA-PBE exchange–correlation functional is used for calculation. The pseudopotentials are selected as OTFG (On The Fly Generated) Ultrasoft. The Brillouin zone integral of the mineral surface adopts the Monkhorst–Pack K-point grid sampling of (2 × 2 × 1). The truncation of the plane wave can be set to 400 eV. The convergence value of SCF (Self-Consistent Field) is determined to be 2.0×10^{-6} eV per atom. The BFGS (Broyden–Fletcher–Goldfarb–Shanno) algorithm is adopted for properties such as geometric optimization (inversion space), atomic force and atomic displacement. The convergent tolerance for structural optimization and energy calculation is set as: the energy convergence threshold is 2.0×10^{-5} eV per atom, the convergence threshold of interatomic force is 0.05 eV $Å^{-1}$, the convergence threshold of atomic displacement is 0.002 Å, and the convergence threshold of internal stress in the crystal is 0.1 GPa.

2.2.2 Calculation method of adsorption energy. The differences in the adsorption of WO_4^{2-} on different clay mineral (001) surfaces can be evaluated by adsorption energy (E_{ads}), and the calculation method of E_{ads} is shown in formula (2):

$$E_{ads} = E_{Surface/Adsorbate} - E_{Adsorbate} - E_{Surface} \quad (2)$$

In the formula, E_{ads} represents the adsorption energy of WO_4^{2-} on the (001) plane of the mineral. $E_{Surface/Adsorbate}$ is the total energy of the system after WO_4^{2-} adsorption on the (001) plane of the mineral. $E_{Adsorbate}$ denotes the total energy of WO_4^{2-} before adsorption, and $E_{Surface}$ stands for the total energy of the mineral's (001) plane before adsorption. The lower the adsorption energy, the more stable the WO_4^{2-} adsorption on the mineral (001) plane.

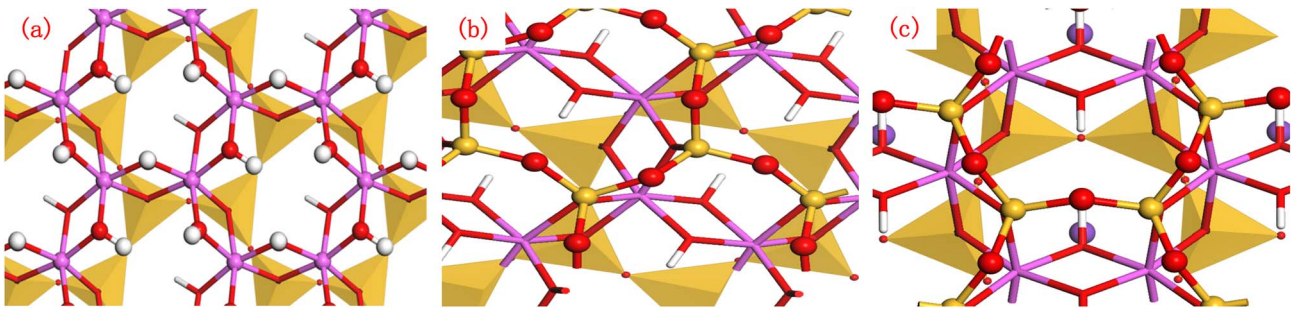

Fig. 1 Structural models of kaolinite (001) surface (a), montmorillonite (001) surface (b), and potassium illite (001) surface (c).

3 Results and discussion

3.1 Adsorption test

3.1.1 The influence of time on adsorption. The adsorption process is significantly time-dependent, with its kinetic characteristics, equilibrium state, and underlying mechanisms all influenced by time. As the reaction proceeds, the active sites on the adsorbent surface are gradually occupied until saturation is reached, while the remaining adsorption capacity becomes progressively depleted, leading to a minimum in adsorption efficiency. Understanding the impact of time on the adsorption of WO_4^{2-} onto different clay minerals facilitates accurate predictions of tungsten migration in soil-plant systems. This provides a scientific basis for soil pollution remediation and environmental risk assessment. To study the effect of contact time on WO_4^{2-} adsorption, experiments were conducted with the initial WO_4^{2-} concentration fixed at 100 mg L^{-1} and pH = 5. The adsorption of WO_4^{2-} onto various clay minerals was investigated, and the results are shown in Fig. 2.

Fig. 2 directly illustrates the curves of adsorption capacity over time for the three clay minerals. During the initial adsorption stage, all three minerals show a sharp increase in adsorption capacity. Illite has the fastest adsorption rate but the lowest capacity. In the early stage, the rate at which kaolinite adsorbs WO_4^{2-} exceeds that of montmorillonite. As time extends, the adsorption capacity of clay minerals for WO_4^{2-} peaks and fluctuates within a range, indicating adsorption saturation and stability. At the end of adsorption, montmorillonite shows the highest equilibrium adsorption capacity at 15.99 mg g^{-1}, followed by kaolinite at 12.60 mg g^{-1} and illite at 8.21 mg g^{-1}. Thus, the adsorption capacity order is: montmorillonite > kaolinite > illite.

3.1.2 The influence of concentration on adsorption. The WO_4^{2-} concentration is a key factor in its adsorption on clay minerals. It affects the occupation of active sites, adsorption driving force, and mechanism. Within the range of low initial concentrations, the adsorption capacity increases significantly as the initial concentration rises, which is likely due to the fact that the active sites on the adsorbent surface are not yet fully occupied.[31,32] At moderate concentrations, active site occupation slows the adsorption capacity growth. At high concentrations, near-saturation stabilizes adsorption capacity. With a fixed pH of 5 and 12-hour adsorption time, experiments on kaolinite, montmorillonite, and illite adsorption of WO_4^{2-} were carried out, and the results are shown in Fig. 3.

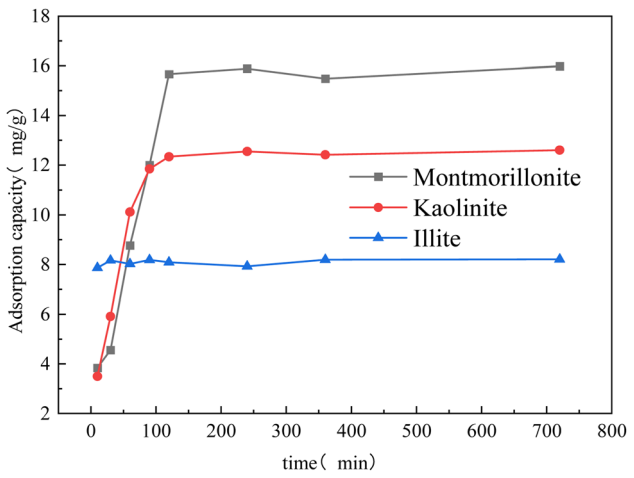

Fig. 2 The influence of time on the adsorption of WO_4^{2-} by clay minerals.

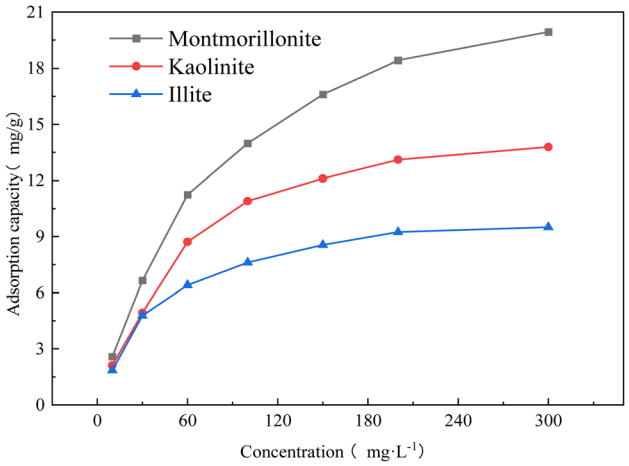

Fig. 3 The influence of initial concentration on the adsorption of WO_4^{2-} by clay minerals.

Fig. 3 shows the trends in the adsorption capacity of three clay minerals for WO_4^{2-} as a function of concentration. Over the range of 0–300 mg L^{-1}, the adsorption capacity of kaolinite, montmorillonite, and illite for WO_4^{2-} increases with rising WO_4^{2-} concentration; however, this rate of increase gradually slows as active sites on the clay mineral surfaces become occupied. Illite's adsorption capacity approaches its maximum value with only slight further increases, whereas montmorillonite's adsorption capacity is less affected and continues to rise steadily with increasing WO_4^{2-} concentration. The maximum adsorption capacities of the three clay minerals across the tested concentration range are as follows: montmorillonite at 19.93 mg g^{-1}, kaolinite at 13.79 mg g^{-1}, and illite at 9.50 mg g^{-1}. Montmorillonite thus exhibits the most superior adsorption performance, with the final adsorption capacities following the order: illite < kaolinite < montmorillonite.

3.1.3 The influence of pH on adsorption. The solution pH significantly affects tungsten adsorption in soils by influencing the surface charge of clay minerals, thereby impacting tungsten adsorption efficiency. It is a key factor in the adsorption and desorption of WO_4^{2-} by clay minerals. Different clay minerals have varying surface charge types and pH sensitivities. To explore this relationship, experiments were conducted at a fixed initial WO_4^{2-} concentration of 100 mg L^{-1} and an adsorption time of 24 hours. The results, presented in Fig. 4, show how WO_4^{2-} adsorption by different clay minerals varies with pH.

Fig. 4 shows the adsorption of WO_4^{2-} by clay minerals at different pH levels. At pH 3, all three minerals—montmorillonite, kaolinite, and illite—exhibit maximum adsorption capacities of 19.162 mg g^{-1}, 15.932 mg g^{-1}, and 8.108 mg g^{-1},

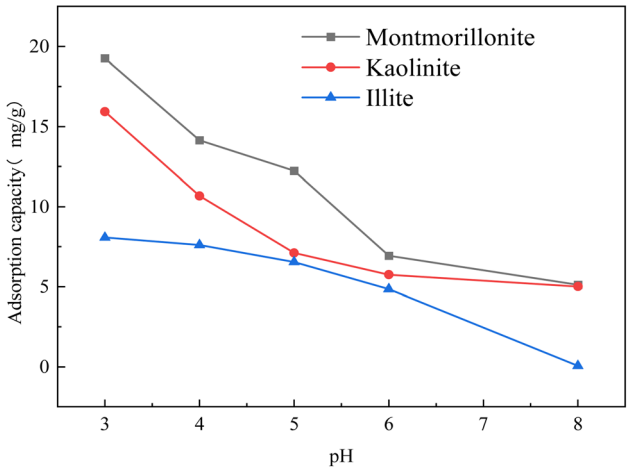

Fig. 4 The influence of pH on the adsorption of WO_4^{2-} by clay minerals.

respectively. Thus, the adsorption capacity order is montmorillonite > kaolinite > illite. As pH increases, the adsorption capacity decreases. This is because when the solution pH exceeds 4, the clay minerals' surfaces release H atoms, stabilizing the solution pH at around 4 and increasing the surface negative charge. The resulting electrostatic repulsion between the minerals and WO_4^{2-} reduces adsorption. At pH 8, the adsorption capacities drop to 5.122 mg g^{-1} for montmorillonite, 5.011 mg g^{-1} for kaolinite, and 0.058 mg g^{-1} for illite.

3.2 Adsorption kinetics

Adsorption kinetic models, crucial for understanding and predicting adsorption processes, describe the adsorption rate and time-dependent changes. They aid in optimizing adsorption design, setting process parameters, and selecting adsorbent materials. The pseudo-first-order and pseudo-second-order kinetic models are widely used. The pseudo-first-order model, derived from Lagergren's equation, assumes that the adsorption rate is governed by the equilibrium between surface adsorption and desorption. In contrast, the pseudo-second-order model accounts for chemisorption or electron-sharing processes, as well as interactions between the adsorbent and adsorbate throughout the entire process. This study explores the adsorption kinetics of WO_4^{2-} onto montmorillonite, kaolinite, and illite. Adsorption data at different time points was collected and fitted to these two models to determine kinetic parameters. The goal is to reveal the adsorption rate characteristics and mechanisms of the three minerals for WO_4^{2-}, offering theoretical and technical guidance for using clay minerals in WO_4^{2-} pollution control. The model results and fitting parameters are shown in Fig. 5 and Table 2.

As shown in Fig. 5 and Table 2, the pseudo-second-order kinetic model has higher R^2 values than the pseudo-first-order model for the adsorption of WO_4^{2-} onto montmorillonite, kaolinite, and illite. This suggests that the pseudo-second-order model better fits the adsorption behavior of these minerals toward WO_4^{2-}. The pseudo-second-order model considers the entire adsorption process, where the rate is influenced by the concentration of the adsorbate and may involve multiple adsorption sites and chemical interactions. From the pseudo-second-order model, the adsorption rates of WO_4^{2-} for montmorillonite, kaolinite, and illite are 0.0014, 0.0042, and 0.0717 mg g^{-1} min^{-1}, respectively. Thus, the adsorption rate order is illite > kaolinite > montmorillonite, with illite reaching equilibrium first. The equilibrium adsorption capacities (q_e) are 17.19 mg g^{-1} for montmorillonite, 13.03 mg g^{-1} for kaolinite, and 8.21 mg g^{-1} for illite. Therefore, the final adsorption capacity order is montmorillonite > kaolinite > illite, indicating montmorillonite has the best adsorption performance for WO_4^{2-}.

3.3 Adsorption isotherm

Adsorption isotherms are curves that describe the relationship between adsorbate concentration and adsorption capacity at

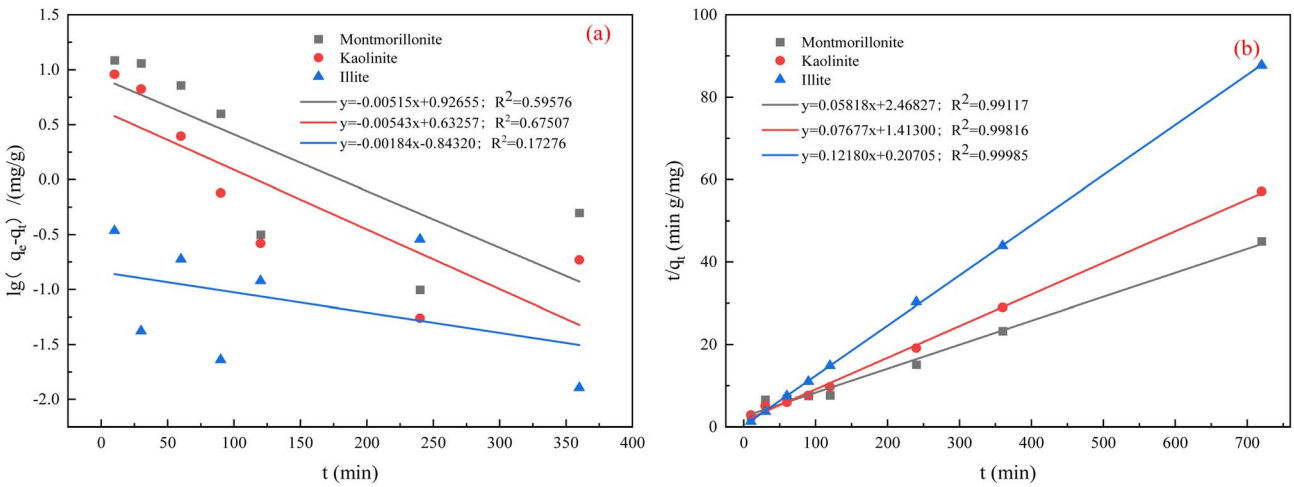

Fig. 5 (a) Quasi-first-order kinetic models of adsorption of WO_4^{2-} by three clay minerals; (b) quasi-second-order kinetic models of adsorption of WO_4^{2-} by three clay minerals.

Table 2 Kinetic fitting parameters of WO_4^{2-} adsorption by three clay minerals[a]

	W(VI)		Quasi-first-order dynamic model			Quasi-second-order dynamic model	
Sample	C_0 (mg L^{-1})	q_e (mg g^{-1})	K_1 (min^{-1})	R^2	q_e (mg g^{-1})	K_2 (mg g^{-1} min^{-1})	R^2
Montmorillonite	100	8.44	0.0119	0.59576	17.19	0.0014	0.99117
Kaolinite	100	4.29	0.0125	0.67507	13.03	0.0042	0.99816
Illite	100	6.97	0.0042	0.17276	8.21	0.0717	0.99985

[a] In the table, C_0 is the initial adsorption concentration, q_e is the adsorption capacity at equilibrium, K_1 is the quasi-first-order kinetic rate constant, K_2 is the quasi-second-order kinetic rate constant, and R^2 is the coefficient of determination.

equilibrium under constant temperature. They aid in evaluating an adsorbent's capacity for a specific adsorbate and provide data for thermodynamic and kinetic analyses. The Langmuir model, which assumes monolayer adsorption on a uniform surface with no intermolecular interactions, is well-suited for such processes. In contrast, the Freundlich model is empirical and applies to multilayer adsorption or adsorption on heterogeneous surfaces.[33] In this study, adsorption data of WO_4^{2-} solutions with varying initial concentrations onto three clay minerals were used to construct Langmuir and Freundlich isotherm curves (Fig. 6). By fitting and analyzing these models, we can gain a comprehensive understanding of WO_4^{2-} adsorption characteristics on the three minerals, uncover the adsorption mechanisms, and compare the adsorption performance of different minerals toward WO_4^{2-}.

Fig. 6 shows the Langmuir and Freundlich adsorption isotherm models of the adsorption behavior of WO_4^{2-} by three clay minerals. The relevant isothermal parameters are presented in Table 3. When evaluating the applicability of these two models, the correlation coefficient R^2 is a key indicator, which can provide a more intuitive understanding of which model can describe the adsorption process more accurately. By fitting the isothermal models of WO_4^{2-} adsorption of three clay minerals, it was found that both the Langmuir model and the Freundlich model could explain the adsorption behavior of WO_4^{2-}, but the correlation coefficient R_L^2 of the Langmuir model was greater than that R_F^2 of the Freundlich model. It indicates that the Langmuir model can be better used to explain the adsorption behavior of WO_4^{2-} on the surface of clay minerals. According to the Langmuir equation calculation, the

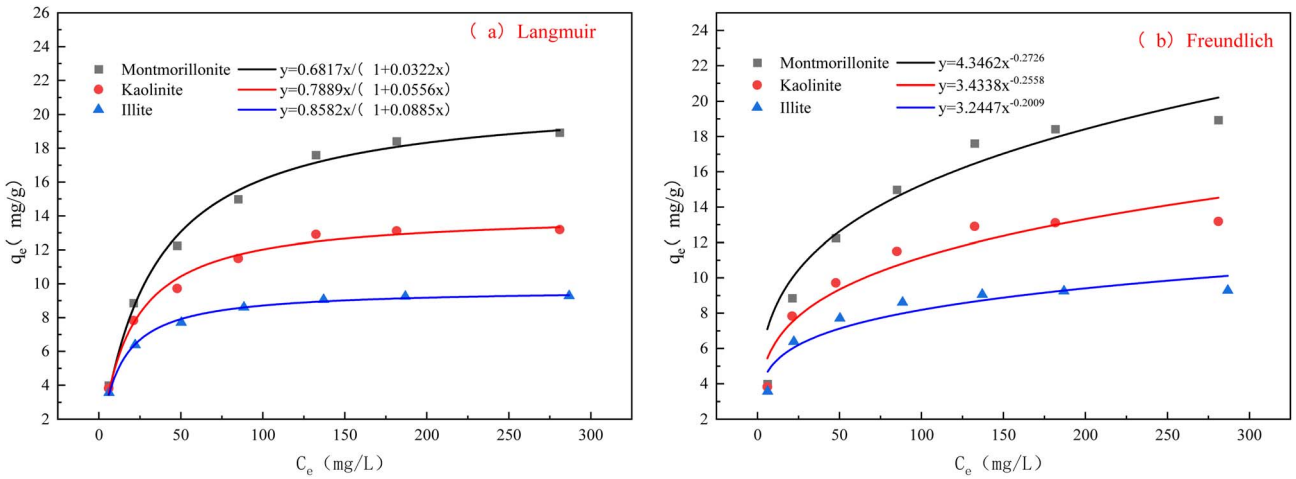

Fig. 6 (a) Langmuir models of adsorption of WO_4^{2-} by three clay minerals; (b) Freundlich model of adsorption of WO_4^{2-} by three clay minerals.

Table 3 Fitting parameters of the Langmuir model and the Freundlich model[a]

	Langmuir model			Freundlich model		
Sample	q_{max} (mg g^{-1})	K_L (L mg^{-1})	R_L^2	K_F (L g^{-1})	n	R_F^2
Montmorillonite	21.18	0.0322	0.9914	4.3462	0.2726	0.9328
Kaolinite	14.18	0.0556	0.9882	3.4338	0.2558	0.8968
Illite	9.70	0.0885	0.9962	3.2447	0.2009	0.8684

[a] In the table, q_{max} is the maximum adsorption capacity, K_L is the Langmuir equilibrium constant, K_F is the Freundlich constant, n is the Freundlich exponent, and R^2 is the coefficient of determination.

equilibrium adsorption capacities of WO_4^{2-} by montmorillonite, kaolinite and illite are 21.18 mg g^{-1}, 14.18 mg g^{-1} and 9.70 mg g^{-1} respectively. The adsorption equilibrium constants K_L are 0.03 L mg^{-1}, 0.06 L mg^{-1}, and 0.09 L mg^{-1}. It indicates that the adsorption capacity of the three clay minerals for WO_4^{2-} at adsorption equilibrium is: montmorillonite > kaolinite > illite. In addition, the n value (adsorption capacity index) in the Freundlich adsorption model is used as an indicator to measure the strength of adsorbing heavy metals. The larger the n value, the better the adsorption performance. The n values of adsorbing WO_4^{2-} by montmorillonite, kaolinite and illite are relatively small, which are 0.27, 0.26 and 0.20 respectively. It indicates that the adsorption of WO_4^{2-} by montmorillonite, kaolinite and illite is relatively difficult.

3.4 First-principles study on the adsorption of WO_4^{2-} on different clay mineral (001) surfaces

3.4.1 Analysis of adsorption energy and structural parameters of WO_4^{2-} on different clay mineral (001) surfaces. To discuss the adsorption differences of WO_4^{2-} in three different clay minerals, namely kaolinite, montmorillonite and illite, Fig. 7 shows the adsorption equilibrium configurations of WO_4^{2-} on the (001) surface of kaolinite, montmorillonite and potassium illite (001) surface respectively. The numbers in the figure represent the bond length values, with the unit of Å. Table 4 shows the adsorption energy and structural parameters of WO_4^{2-} on the kaolinite (001) surface, montmorillonite (001) surface and potassium illite (001) surface. It can be known from Fig. 7 and Table 4 that one O atom in WO_4^{2-} is adsorbed on the kaolinite (001) surface by forming an Al–O coordination bond with one Al atom on the kaolinite (001) surface, and the bond length of the Al–O coordination bond is 1.889 Å. On the (001) face of montmorillonite and the (001) face of potassium illite, the two O atoms in WO_4^{2-} are adsorbed on the mineral surface by forming Si_1–O_1 and Si_2–O_2 coordination bonds with the two Si atoms on the (001) face of montmorillonite and the (001) face of potassium illite. The bond lengths of the Si_1–O_1 and Si_2–O_2 coordination bonds formed by the adsorption of WO_4^{2-} on the (001) face of montmorillonite are 1.799 Å and 1.889 Å, respectively, and those formed by the adsorption of WO_4^{2-} on the (001) face of potassium illite are 1.800 Å and 1.800 Å.

The adsorption of WO_4^{2-} on the (001) surfaces of kaolinite, montmorillonite, and potassium illite is chemical. With an adsorption energy of −178.52 kJ mol^{-1}, WO_4^{2-} is most stable on montmorillonite (001). Next is kaolinite (001) at −166.94 kJ mol^{-1}, and then potassium illite (001) at −112.65 kJ mol^{-1}, indicating the weakest adsorption there. Overall, WO_4^{2-} adsorption strength on the three clay minerals ranks as: montmorillonite (001) > kaolinite (001) > potassium illite (001).

3.4.2 Electronic density of states analysis of the adsorption effect of WO_4^{2-} on the (001) surface of different clay minerals. Fig. 8 presents the density of states (DOS) distribution curves for

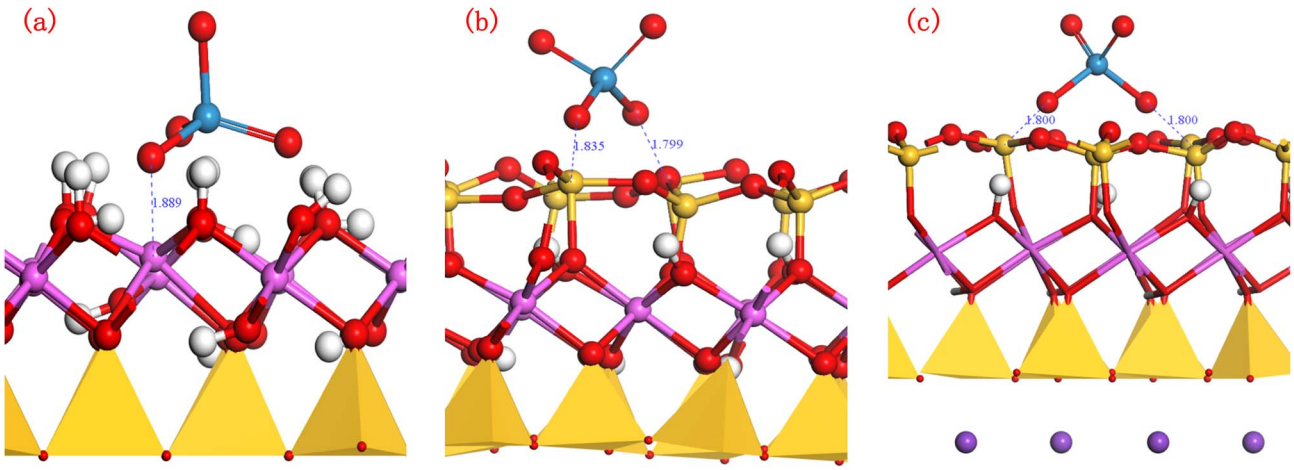

Fig. 7 Adsorption equilibrium configuration diagrams of WO_4^{2-} on kaolinite (001) surface (a), montmorillonite (001) surface (b), and potassium illite (001) surface (c).

Table 4 Adsorption energy and structural parameters of WO_4^{2-} on the kaolinite (001) surface, montmorillonite (001) surface, and potassium illite (001) surface

Adsorption configuration	N_{M-O}[a]	R_{M-O}[b]/Å	$R_{La-O\ mean}$[c]/Å	E_{ads}[d]/kJ mol^{-1}
WO_4^{2-}—kaolinite (001) surface	1	1.889	1.889	−166.94
WO_4^{2-}—montmorillonite (001) surface	2	1.835, 1.799	1.817	−178.52
WO_4^{2-}—illite (001) surface	2	1.800, 1.800	1.800	−112.65

[a] M–O number of bonds. [b] M–O key length. [c] M–O average key length. [d] Adsorption energy.

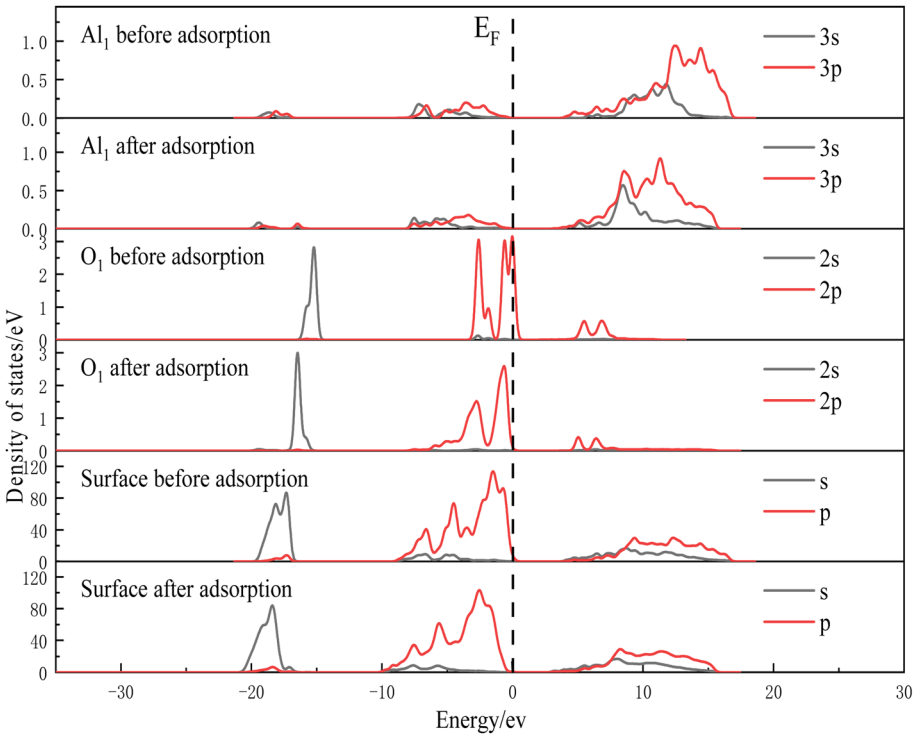

Fig. 8 Al–O atoms and surface state densities of WO_4^{2-} before and after adsorption on the kaolinite (001) surface.

WO_4^{2-} adsorbed on the kaolinite (001) surface, with the Fermi level (E_F) set to zero (marked by a vertical dashed line). O_1 is the WO_4^{2-} atom bonding with kaolinite, and Al_1 is the kaolinite surface atom bonding with O_1. The DOS near the Fermi level for Al_1 mainly comes from its 3p states, while for O_1, it mainly comes from its 2p states. After adsorption, the DOS of Al_1 and O_1 shift left to lower energies, and the kaolinite surface DOS also moves to lower energies. The 2p states of O_1 become more non-localized post-adsorption, while the 2s and 2p states of Al_1 remain non-localized with little change. New, weak peaks appear for O_1's 2s and 2p orbitals at −19.5 eV and Al_1's 3s and 3p orbitals at −16.4 eV, suggesting hybridization between Al_1 and O_1.

Table 5 presents the Mulliken population analysis of Al_1 and O_1 in WO_4^{2-} before and after adsorption on the kaolinite (001) surface. After adsorption, O_1 loses electrons from its 2s orbital and gains electrons in its 2p orbital, gaining 0.05 electrons overall (charge changes from −0.89 to −0.94). Al_1 mainly loses electrons from its 3p orbital, losing 0.03 electrons overall (charge changes from 1.82 to 1.85).

Table 5 Mulliken charge distribution of Al–O atoms before and after adsorption of WO_4^{2-} on the kaolinite (001) surface

Species	s	p	d	f	Total	Charge/*e*
Al_1 before	0.47	0.71	0.00	0.00	1.18	1.82
Al_1 after	0.47	0.68	0.00	0.00	1.15	1.85
Charge	0.00	−0.03	0.00	0.00	−0.03	0.03
O_1 before	1.90	4.99	0.00	0.00	6.89	−0.89
O_1 after	1.87	5.07	0.00	0.00	6.94	−0.94
Charge	−0.03	0.08	0.00	0.00	0.05	−0.05

Fig. 9 shows the density of states distribution curves of WO_4^{2-} atoms before and after adsorption on the montmorillonite (001) surface. The energy of E_F at the Fermi level is set as zero (indicated by the vertical dotted line in the figure). Among them, O_1 and O_2 atoms are the atoms in WO_4^{2-} that form bonds with the surface of montmorillonite, while Si_1 and Si_2 atoms are the atoms on the surface of montmorillonite that form bonds with O_1 and O_2. It can be seen from the figure that the density of states of Si_1 and Si_2 atoms near the Fermi level is mainly contributed by the 3p state, while the density of states of O_1 and O_2 atoms near the Fermi level is mainly contributed by the 2p state. After adsorption, the densities of states of Si_1 and Si_2 atoms and O_1 and O_2 atoms move as a whole to the left low-energy direction, indicating that the electron cloud density of Si–O atoms increases relatively. The binding energy of electrons decreases and the interaction of Si–O atoms increases. The localization of the 2p state of O_1 and O_2 atoms before adsorption is very strong. After adsorption, the 2p state at the Fermi level changes from a narrow peak to a wide peak, and the double peak becomes multiple peaks, indicating that the non-localization of O_1 and O_2 is enhanced. However, the peak density of the 3s state of Si_1 and Si_2 atoms decreases, the localization of electrons weakens, and the non-localization is enhanced. New peaks were formed at the 3p orbitals of the Si_1 atom at −17.1 eV and 6.4 eV, the 3p orbitals of the Si_2 atom at −16.9 eV and 6.4 eV, the 2p orbitals of the O_1 and O_2 atoms at −4.6 eV and 4.4 eV, and the 2s orbitals at −19.6 eV. It indicates that the Si_1–O_1 and Si_2–O_2 atoms have undergone hybridization reactions.

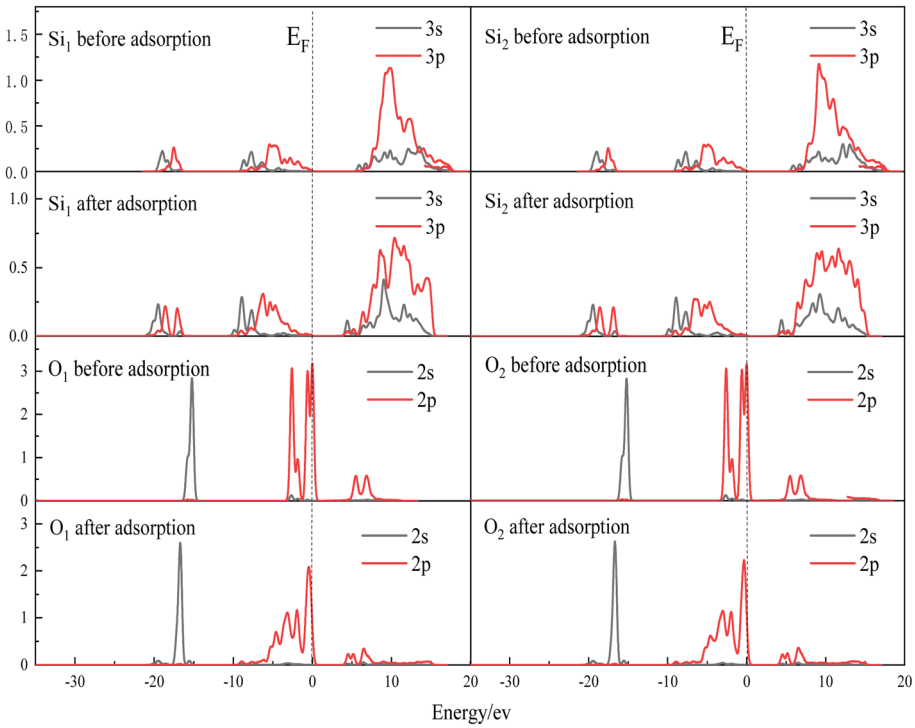

Fig. 9 Si–O atomic state densities of WO_4^{2-} before and after adsorption on the (001) surface of montmorillonite.

Table 6 Mulliken charge distribution of Si–O atoms before and after adsorption of WO_4^{2-} on the (001) surface of montmorillonite

Species	s	p	d	f	Total	Charge/*e*
Si_1 before	0.61	1.12	0.00	0.00	1.73	2.27
Si_1 after	0.66	1.21	0.00	0.00	1.87	2.13
Charge	0.05	0.09	0.00	0.00	0.14	−0.14
Si_2 before	0.60	1.12	0.00	0.00	1.72	2.28
Si_2 after	0.67	1.22	0.00	0.00	1.89	2.11
Charge	0.07	0.10	0.00	0.00	0.17	−0.17
O_1 before	1.90	4.98	0.00	0.00	6.88	−0.88
O_1 after	1.86	5.00	0.00	0.00	6.86	−0.86
Charge	−0.04	0.02	0.00	0.00	−0.02	0.02
O_2 before	1.90	4.99	0.00	0.00	6.89	−0.89
O_2 after	1.86	4.99	0.00	0.00	6.85	−0.85
Charge	−0.04	0.00	0.00	0.00	−0.04	0.04

From the analysis of the Mulliken charge distribution of Si–O atoms before and after the adsorption of WO_4^{2-} on the montmorillonite (001) surface in Table 6, it can be known that after adsorption, the O_1 and O_2 atoms mainly lose electrons in the 2s orbital and gain electrons in the 2p orbital. The O_1 atom loses 0.04 electrons in the 2s orbital and gains 0.02 electrons in the 2p orbital, losing 0.02 electrons overall. The charge changes from −0.88 to −0.86. The O_2 atom lost 0.04 electrons in the 2s orbital, losing 0.04 electrons as a whole, and its charge changed from −0.89 to −0.85. The Si_1 and Si_2 atoms mainly gain electrons in the 3s and 3p orbitals. The Si_1 atom gains 0.05 electrons in the 3s orbital and 0.09 electrons in the 3p orbital. Overall, it gains 0.14 electrons, and the charge changes from 2.27 to 2.13. The Si_2 atom gains 0.07 electrons in the 3s orbital, 0.10 electrons in the 3p orbital, and a total of 0.17 electrons, with the charge changing from 2.28 to 2.11.

Fig. 10 shows the density of states distribution curves of WO_4^{2-} atoms before and after adsorption on the potassium illite (001) surface. The energy of E_F at the Fermi level is set as zero (indicated by the vertical dotted line in the figure). Among them, the O_1 and O_2 atoms are the atoms in WO_4^{2-} that form bonds with the illite surface, and the Si_1 and Si_2 atoms are the atoms on the illite surface that form bonds with the O_1 and O_2 atoms. It can be seen from the figure that the density of states of Si_1 and Si_2 atoms near the Fermi energy level is mainly contributed by the 3p state, while the density of states of O_1 and O_2 atoms near the Fermi energy level is mainly contributed by the 2p state. After adsorption, the densities of states of O_1 and O_2 atoms shift significantly to the left low-energy direction overall, indicating that the electron binding energy of Si–O atoms decreases and the interaction increases. The localization of the 3p state of Si_1 and Si_2 atoms before adsorption is very strong. After adsorption, the 3p state at the Fermi level changes from a narrow peak to a wide peak, and the double peak becomes a continuous peak. However, the intensity of the 2s and 2p orbital peaks of O_1 and O_2 atoms after adsorption decreases, and the range of state density peaks widens, indicating that the electronic localization of Si and O atoms weakens and the non-localization is enhanced. The Si_1 and Si_2 atoms are at −21.1 eV and −11.8 eV in the 3s orbital, and at −21.0 eV, 0.43 eV and 1.61 eV in the 3p orbital. The O_1 and O_2 atoms are at −23.4 eV, −19.9 eV and 1.64 eV in the 2s orbital. New peaks were formed at −10.2 eV and 0.81 eV in the 2p

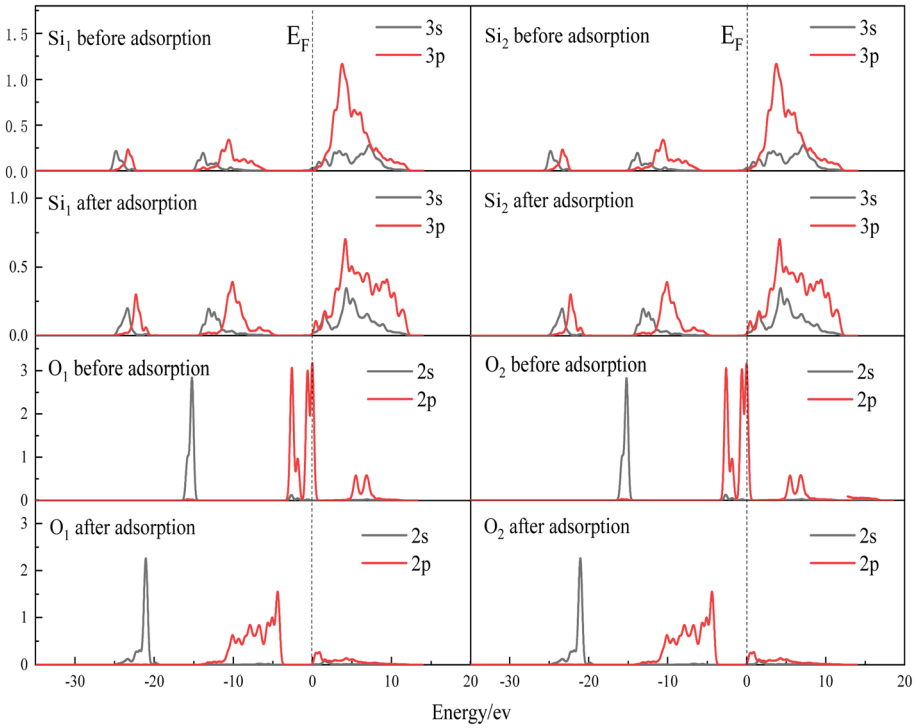

Fig. 10 Si–O atomic state densities before and after adsorption of WO_4^{2-} on the potassium illite (001) surface.

Table 7 Mulliken charge distribution of Si–O atoms before and after adsorption of WO_4^{2-} on the potassium illite (001) surface

Species	s	p	d	f	Total	Charge/*e*
Si_1 before	0.62	1.12	0.00	0.00	1.74	2.26
Si_1 after	0.67	1.21	0.00	0.00	1.88	2.12
Charge	0.05	0.09	0.00	0.00	0.14	−0.14
Si_2 before	0.62	1.12	0.00	0.00	1.74	2.26
Si_2 after	0.67	1.21	0.00	0.00	1.88	2.12
Charge	0.05	0.09	0.00	0.00	0.14	−0.14
O_1 before	1.90	4.99	0.00	0.00	6.89	−0.89
O_1 after	1.83	5.05	0.00	0.00	6.88	−0.88
Charge	−0.07	0.06	0.00	0.00	−0.01	0.01
O_2 before	1.90	4.99	0.00	0.00	6.89	−0.89
O_2 after	1.83	5.05	0.00	0.00	6.88	−0.88
Charge	−0.07	0.06	0.00	0.00	−0.01	0.01

orbital, indicating that hybridization reactions occurred in the Si_1–O_1 and Si_2–O_2 atoms.

From the analysis of the Mulliken charge distribution of Si–O atoms before and after the adsorption of WO_4^{2-} on the potassium illite (001) surface in Table 7, it can be known that after adsorption, O_1 and O_2 atoms mainly lose electrons in the 2s orbital and gain electrons in the 2p orbital. O_1 and O_2 atoms lose 0.07 electrons in the 2s orbital of O_1 and O_2 atoms and gain 0.06 electrons in the 2p orbital. The whole loses 0.01 electrons and the charge changes from −0.89 to −0.88. Both Si_1 and Si_2 atoms gain electrons in the 3s and 3p orbitals. Si_1 and Si_2 atoms gain 0.05 electrons in the 3s orbital and 0.09 electrons in the 3p orbital. As a whole, they gain 0.14 electrons, and the charge changes from 2.26 to 2.12.

4 Conclusion

The differences in tungsten adsorption behaviors of different clay minerals (kaolinite, montmorillonite, illite) were studied by combining first-principles simulation based on density functional theory with experiments. The research results show that:

(1) Adsorption tests show that reducing the pH value of the solution, increasing the initial concentration and adsorption time are conducive to the adsorption of WO_4^{2-} on the surface of the three clay minerals. With the increase of pH, H atoms are released on the surface of the clay minerals, increasing the negative charge carried on the surface of the clay minerals, and the electrostatic repulsion between the minerals and WO_4^{2-} also continuously increases. The adsorption capacity of WO_4^{2-} decreases with the increase of pH. The adsorption capacity of the three clay minerals for WO_4^{2-} from large to small is: montmorillonite > illite > kaolinite.

(2) The studies of adsorption kinetics and adsorption isotherms show that the adsorption of WO_4^{2-} on the surfaces of three clay minerals is more in line with the quasi-second-order kinetics and Langmuir model, and the adsorption is mainly chemical adsorption. The adsorption rates of WO_4^{2-} by the three clay minerals from high to low are: illite > kaolinite > montmorillonite. Illite reaches adsorption equilibrium first. At adsorption equilibrium, the adsorption amounts of WO_4^{2-} by the three clay minerals are: montmorillonite > kaolinite > illite.

(3) One O atom in WO_4^{2-} is adsorbed on the kaolinite (001) surface by forming an Al–O coordination bond with one Al atom on the kaolinite (001) surface. The bond length of the Al–O coordination bond is 1.889 Å. On the (001) face of

montmorillonite and the (001) face of potassium illite, the two O atoms in WO_4^{2-} are adsorbed on the mineral surface by forming Si_1–O_1 and Si_2–O_2 coordination bonds with the two Si atoms on the (001) face of montmorillonite and the (001) face of potassium illite. The bond lengths of the Si_1–O_1 and Si_2–O_2 coordination bonds formed by the adsorption of WO_4^{2-} on the (001) face of montmorillonite are 1.799 Å and 1.889 Å, respectively, and those formed by the adsorption of WO_4^{2-} on the (001) face of potassium illite are 1.800 Å and 1.800 Å, respectively.

(4) The first-principles study shows that the adsorption of WO_4^{2-} on the kaolinite (001) surface, montmorillonite (001) surface and potassium illite (001) surface is mainly chemical adsorption, and the adsorption energies are −166.94 kJ mol^{-1}, −178.52 kJ mol^{-1} and −112.65 kJ mol^{-1} respectively. It indicates that the adsorption energy of WO_4^{2-} on the (001) surface of montmorillonite is the lowest, the structure is the most stable, and it is the easiest to adsorb on the (001) surface of montmorillonite, followed by the (001) surface of kaolinite. WO_4^{2-} is the most difficult to adsorb on the (001) surface of potassium illite.

Conflicts of interest

The authors declare that they have no known competing financial interests or personal relationships that could have appeared to influence the work reported in this paper.

Data availability

Due to ethical restrictions, the raw data cannot be made publicly available. However, de-identified data may be obtained from the corresponding author upon reasonable request.

Acknowledgements

This work was funded by the National Key R&D Program of China [no. 2019YFC1805100], the National Natural Science Foundation of China [no. 51664025], the Jiangxi Provincial Natural Science Foundation [no. 20232ACB203026], the Science and Technology Project of Ganzhou City [no. 2023PNS27982], Jiangxi Provincial Key Laboratory of Environmental Pollution Prevention and Control in Mining and Metallurgy [no. 2023SSY01071].

References

1 P. Beiersdorfer, J. Clementson and U. I. Safronova, *Atoms*, 2015, **3**, 260–272, DOI: **10.3390/atoms3020260**.
2 A. Barua, S. Pradhan, M. Priyadarshini, A. Patra and K. Kumari, *J. Mater. Eng. Perform.*, 2024, **34**, 8232–8252, DOI: **10.1007/s11665-024-09490-8**.
3 G. Awasthi, K. Santhy, N. Jamnapara, S. Agrawal, D. Mandal, M. Salot and S. K. Chaudhury, *J. Mater. Sci.: Mater. Electron.*, 2025, **36**, 1–16, DOI: **10.1007/s10854-024-14101-2**.
4 Z. Huang, Z. Huang and X. Zu, *J. Phys.: Conf. Ser.*, 2023, **2541**, 012042, DOI: **10.1088/1742-6596/2541/1/012042**.
5 Y. J. He, W. J. Wang, Y. W. Chen, J. Hua, C. N. Deng and H. S. Li, *Sci. Total Environ.*, 2024, **906**, 167437, DOI: **10.1016/j.scitotenv.2023.167437**.
6 T. Mikuszewski, A. Tomaszewska, G. Moskal, D. Migas and B. Witala, *J. Min. Metall., Sect. B*, 2022, **58**, 179–189, DOI: **10.2298/JMMB211107002M**.
7 A. M. Plyusnin, Yu. S. Voronina, A. V. Ukraintsev, M. K. Chernyavskii, E. G. Peryazeva and E. P. Chebykin, *Geochem. Int.*, 2023, **61**, 1293–1307, DOI: **10.1134/S0016702923110095**.
8 I. Timofeev, N. Kosheleva and N. Kasimov, *Sci. Total Environ.*, 2018, **642**, 63–76, DOI: **10.1016/j.scitotenv.2018.06.042**.
9 Y. X. Wang, B. J. Nie, S. L. Zheng, H. Y. Wu, N. Chen and D. Z. Wang, *Environ. Int.*, 2024, **188**, 108774, DOI: **10.1016/j.envint.2024.108774**.
10 X. J. Zheng, Z. Q. Wang, Q. Li, L. L. Liu and M. Chen, *Ecol. Eng.*, 2025, **213**, 107565, DOI: **10.1016/j.ecoleng.2025.107565**.
11 A. M. Plyusnin, Yu. S. Voronina, A. V. Ukraintsev, M. K. Chernyavskii, E. G. Peryazeva and E. P. Chebykin, *Geochem. Int.*, 2023, **61**, 1293–1307, DOI: **10.1134/S0016702923110095**.
12 N. V. Reutova, T. V. Reutova, F. R. Dreeva and A. V. Shevchenko, *Environ. Geochem. Health*, 2022, **44**, 4557–4568, DOI: **10.1007/s10653-022-01221-z**.
13 J. L. Clausen and N. Korte, *Sci. Total Environ.*, 2009, **407**, 2887–2893, DOI: **10.1016/j.scitotenv.2009.01.029**.
14 P. Steenstra, N. Strigul and J. Harrison, *Chemosphere*, 2020, **242**, 125151, DOI: **10.1016/j.chemosphere.2019.125151**.
15 E. Oburger, C. V. Cid, D. Schwertberger, V. I. K. Reichard and W. W. Wenzel, *Sci. Total Environ.*, 2020, **731**, 139224, DOI: **10.1016/j.scitotenv.2020.139224**.
16 S. Datta, S. E. Vero, G. M. Hettiarachchi and K. G. Scheckel, *Curr. Pollut. Rep.*, 2017, **3**, 55–64, DOI: **10.1007/s40726-016-0046-0**.
17 B. C. Bostick, J. Sun, J. D. Landis and J. L. Clausen, *Environ. Sci. Technol.*, 2018, **52**, 1045–1053, DOI: **10.1021/acs.est.7b05406**.
18 S. Bolan, H. Wijesekara, A. Ireshika, P. Kumar, A. Vithanage, H. Wang, M. Vithanage, T. R. A. Rajapaksha, N. S. Bolan, L. Wang and J. Rinklebe, *Environ. Int.*, 2023, **181**, 108276, DOI: **10.1016/j.envint.2023.108276**.
19 M. Wahsha, C. Bini, E. Argese, S. Minello, F. Fornasier and S. Fontana, *J. Geochem. Explor.*, 2012, **123**, 19–24, DOI: **10.1016/j.gexplo.2012.07.004**.
20 L. Lu, J. Sun, Y. Dai, Y. Zhou, H. Cui, M. Lei and H. Du, *Geochim. Cosmochim. Acta*, 2025, **389**, 1–13, DOI: **10.1016/j.gca.2024.11.032**.
21 G. Petruzzelli and F. Pedron, *Environments*, 2021, **8**, 66, DOI: **10.3390/environments8070066**.
22 G. S. Tuna and W. Braida, *Soil Sediment Contam.*, 2014, **23**, 838–849, DOI: **10.1080/15320383.2014.809049**.
23 T. Iwai and Y. Hashimoto, *Appl. Clay Sci.*, 2017, **143**, 372–377, DOI: **10.1016/j.clay.2017.04.009**.
24 G. Petruzzelli and F. Pedron, *Soil Syst.*, 2020, **4**, 53, DOI: **10.3390/soilsystems4030053**.

25 J. Q. Guo, X. Liao, M. H. Lee, C. W. Kuo, S. T. Huang, W. C. Lin and C. C. Chen, *Appl. Catal., B*, 2019, **243**, 502–512, DOI: **10.1016/j.apcatb.2018.09.089**.
26 V. S. Soldatov, E. G. Kosandrovich and T. V. Bezyazychnaya, *React. Funct. Polym.*, 2018, **131**, 219–229, DOI: **10.1016/j.reactfunctpolym.2018.07.010**.
27 F. S. Vilhena, R. M. Serra, A. V. Boix and M. A. U. Martines, *Comput. Theor. Chem.*, 2016, **1091**, 115–121, DOI: **10.1016/j.comptc.2016.07.017**.
28 C. Suzuki, T. Yaita, S. Suzuki and K. Shiwaku, *J. Phys. Chem. Solids*, 2019, **127**, 169–177, DOI: **10.1016/j.jpcs.2018.11.011**.
29 M. J. He, Y. C. Zhang, X. D. Liu and X. C. Lu, *Inorg. Chem.*, 2025, **64**, 5331–5340, DOI: **10.1021/acs.inorgchem.5c00757**.
30 R. A. Chi and D. Z. Wang, *J. Chin. Soc. Rare Earths*, 1993, **11**, 199–203.
31 F. F. Min, J. Chen and C. L. Peng, *J. China Coal Soc.*, 2018, **43**(01), 242–249, DOI: **10.13225/j.cnki.jccs.2017.4202**.
32 C. L. Peng, F. F. Min, L. Y. Liu and J. Chen, *Appl. Surf. Sci.*, 2016, **387**, 308–316, DOI: **10.1016/j.apsusc.2016.06.079**.
33 M. Vigdorowitsch, A. N. Pchelintsev and L. E. Tsygankova, *Processes*, 2021, **9**, 2227–9717, DOI: **10.3390/pr9071251**.